ASSESSMENT OF A HYBRID EULERIAN-LAGRANGIAN METHOD BY COMPARISON WITH ITS PARENT CODES

Yi Yuan, Politecnico di Milano, Milano, Italy
Luigi Vigevano, Politecnico di Milano, Milano, Italy

Abstract

A hybrid Eulerian-Lagrangian numerical method is developed to simulate the blade-vortex interference of rotorcrafts. The RANS solver ROSITA is used to solve the near-body region covered by Eulerian grids, while a Lagrangian solver developed from DUST is employed for the grid-free farfield to preserve the wake vorticity. The coupling algorithm between the two solvers is such that the sectional aerodynamic loads of lifting bodies integrated from RANS solution are transformed into bound vortex strength of lifting line elements based on Kutta-Joukowski theorem and the induced velocity from all the Lagrangian elements corrects the grid interface boundary in return. The hybrid solver is assessed by three well-documented benchmark cases. The achieved results show good agreement with the experimental data and correlated well with the parent codes' results, demonstrating the capability of vortex preservation and the efficiency of the proposed solver.

1. NOTATION

Symbols

a	Local sound speed, m/s
c	Chord length, m
C_l	Lift coefficient
e	Energy, kg/(ms^2)
$\vec{f}$	Contribution of line vortices to a particle, m^3/s
L	Lift force, N
p	Pressure, kg/(ms^2)
Re	Reynolds number
t	Time, s
$u, \vec{u}$	Velocity, m/s
$\vec{x}$	Position, m
$\vec{\alpha}$	Intensity of a particle, m^3/s
β	Rotor flap angle, °
Γ	Lifting line element intensity, m^2/s
γ	heat capacity ratio
θ	Rotor pitch angle, °
μ	Surface doublet intensity, m^2/s
ν	Dynamic viscosity, m^2/s
ρ	Density, kg/m^3
ψ	Blade azimuth angle, °
b	Body
end, left, right	Position of line vortices
g	Grid
i	Induced, index of particles and wake panels
rel	relative
∞	Infinity

Acronyms:

AOA	Angle of attack
BVI	Blade-vortex interaction
CFD	Computational fluid dynamic
eVTOL	Electric vertical take-off and landing
FBG	Farfield background grid
FMM	Fast multipole method
GCG	Generalized conjugate gradient
MPI	Message Passing Interface
MUSCL	Monotonic upstream-centered scheme for conservation laws
NBG	Near-field background grid
OpenMP	Open multiprocessing
PSE	Particle strength exchange
RANS	Reynolds-averaged Navier-Stokes
ROSITA	Rotorcraft Software ITAly
SA	Spalart-Allmaras
TAAT	Tip Aerodynamic and Acoustics Tests
VPM	Vortex particle method

2. INTRODUCTION

Blade-vortex interaction (BVI) is a critical factor in aerodynamics of the rotorcraft. It occurs when the rotating blades or wings intersect with the wake vortices generated previously. This interaction leads to not only significant aerodynamic loading fluctuations, but also vibrations and increased noise levels which are major concerns for the next-generation urban eVTOL aircraft.

To understand BVI, both classical numerical approaches, Eulerian and Lagrangian, have been developed extensively during the past several decades. From the Eulerian viewpoint, the rapid advancement of computer technology has enabled the development of high-fidelity codes such as OVERFLOW (Ref.1), HMB (Ref.2), and ROSITA (Ref.3). These codes solve unsteady RANS equations, employing a variety of turbulence models, and are applied to problems ranging from 2D airfoil-vortex interactions (Ref.4) to practical full-aircraft simulations (Ref.3). The kinematic of the rotating parts are achieved by CHIMERA technique (Ref.5) or mesh deformation (Ref.6). The fidelity of these codes depends heavily on the grid resolution, necessitating significant computational resources to accurately capture far-field wake vortices and represent BVI. To address this issue, dynamic adaptive gridding (Ref.7), high-order schemes (Ref.8) and vortex confinement methods (Ref.9) augment RANS solvers. But these vortex preservation strategies do not change the essence of the Eulerian methods and usually require greater computational loads.

On the other hand, the Lagrangian method solves a vorticity-velocity formulation of the incompressible Navier-Stokes equations. The lifting bodies (e.g. blades) are modeled into lifting line elements (Ref.10), vortex lattice panels (Ref.11) or surface panels (Ref.12). The wake vortices are generated from the trailing edge of the lifting bodies and represented as vortex filaments (Ref.13) or vortex particles (Ref.14) adopting VPM. The method provides a fast and reliable result, especially a better representation of the far-field wake, and has been applied to complex configurations of eVTOL aircrafts (Ref.15). Nevertheless, fluid compressibility and viscosity are neglected in the assumptions of these models, and some nonlinear aerodynamic phenomenon such as stall effects are accounted for empirically, causing a limited flexibility and engineering-level accuracy.

Taking advantages of the aforementioned two types of approaches, the hybrid Eulerian-Lagrangian method (Refs.16, 17, 18) is emerging recently. The fundamental concept is that the near-body region is solved by Eulerian or RANS part to accurately predict body loads while minimizing the computational requirements, while the far-field wake is convected by the Lagrangian VPM for better vorticity preservation. Several studies have shown the accuracy and efficiency of the hybrid method in simulating hover and forward flight conditions of isolated rotors (Ref.16), as well as more severe BVI cases (Refs.17, 18). However, its application to complicated configurations has not been thoroughly investigated.

In this study, a hybrid Eulerian-Lagrangian method is developed, based on the existing CFD code ROSITA and the mid-fidelity vortex code DUST. The coupling algorithm is designed to keep the consistency between the two solvers' results. The paper is organized as follows. In Section 2, a brief introduction to BVI and state-of-the-art numerical methods is provided. In Section 3, the proposed hybrid solver, including its parent codes and the coupling algorithm, is described. In Section 4, the hybrid solver is validated using three benchmark cases and compared with the results of its parent codes. In Section 5, the capability and advantages of the solver are summarized.

All simulations are performed on 64 cores of two AMD EPYC 7513 CPUs with speed of 2.60GHz on the high-performance cluster of Politecnico di Milano, CFDHub.

3. NUMERICAL METHODS

3.1. Eulerian part

The Eulerian part of the proposed hybrid method adopts ROSITA (Ref.3), which solves unsteady RANS equations coupled with one-equation SA turbulence model (Ref.19), in a system of moving, overset, structured, multi-block grids. The governing equations are discretized spatially using a cell-centered finite volume implementation of Roe's scheme (Ref.20). Second order accuracy is achieved through MUSCL extrapolation supplemented with a modified version of the Van Albada limiter introduced by Venkatakrishnan (Ref.21). Viscous terms are computed via the Gauss theorem and a cell-centered discretization scheme. Time advancement is conducted with a dual-time formulation (Ref.22), involving a second order backward differentiation formula to approximate the time derivative and a fully unfactored implicit scheme in pseudo-time. The GCG together with a block incomplete lower-upper preconditioner, is used

to solve the resulting linear system. The overset grid system is connected by CHIMERA technique, incorporating a modified algorithm from Ref. 23 for enhanced robustness and performance.

3.2. Lagrangian part

The Lagrangian part is developed based on DUST, a medium-fidelity, open-source computational tool designed to efficiently and reliably predict the aerodynamics of unconventional rotorcrafts (Ref.24). The lifting line model is employed to discrete lifting bodies such as blades. The circulation of the lifting line is theoretically derived from tabulated aerodynamic coefficients of the airfoil, yet in the hybrid method the latter are extracted during coupling. Each lifting line element is considered as a uniform-circulation vortex ring and dimensioned by the length of the lifting line segment and the airfoil chord.

The wake shed from the trailing edge of the lifting bodies is initially modelled as vortex lattice elements, whose intensity is obtained enforcing Kutta condition at the trailing edge. These wake panels are then converted into vortex particles after a prescribed number of time steps. The intensity of the particle is integrated from three edges (left, right and end) of corresponding panel and their common edges of the neighboring panels, see Figure 1.

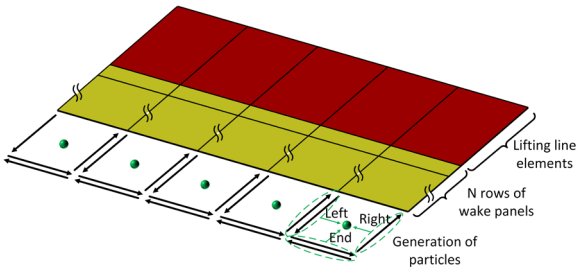

Figure 1: Conversion from wake panels to particles

The contribution of each side is computed as

$$\vec{J}_{\text{left, right}} = \begin{cases} \int \frac{1}{2}\left(\mu_i^t - \mu_{i\pm1}^t\right) d\vec{l}, & \text{if neighbor panel } i \pm 1 \text{ is present} \\ \int \mu_i^t d\vec{l}, & \text{if neighbor panel } i \pm 1 \text{ is absent} \end{cases} \tag{1}$$

$$\vec{J}_{\text{end}} = \int \left(\mu_i^t - \mu_i^{t-1}\right) d\vec{l} \tag{2}$$

and the intensity of the generated particle is the summation of the above ones

$$\vec{\alpha} = \vec{J}_{\text{left}} + \vec{J}_{\text{right}} + \vec{J}_{\text{end}} \tag{3}$$

The radius of each particle is linearly correlated to the radius of the circumscribed circle of the transformed panel. This correlation determines the overlapping ratio of the starting particle distribution.

VPM is used to preserve the wake vorticity in the grid-free farfield region. The vorticity field is expressed by the sum of contributions of vortex particles:

$$\vec{\omega} = \sum_{i=1}^{n} \vec{\alpha}_i(t)\zeta(\vec{x} - \vec{x}_i(t)) \tag{4}$$

The evolution of vorticity field is governed by the discrete equation in convection-diffusion form (Eq.(5)). The first term $\nabla\vec{u}_i(t) \cdot \vec{\alpha}_i(t)$ in the second equation describes the vortex stretching/tilting and is formulated in a transpose scheme, while the second viscosity term $\nu\nabla^2\vec{\alpha}_p(t)$ is solved by PSE method.

$$\begin{cases} \frac{d\vec{x}_i(t)}{dt} = \vec{u}_i(t) \\ \frac{d\vec{\alpha}_i(t)}{dt} = \nabla\vec{u}_i(t) \cdot \vec{\alpha}_i(t) + \nu\nabla^2\vec{\alpha}_i(t) \end{cases} \tag{5}$$

A Cartesian FMM is implemented to accelerate the $\mathcal{O}(N^2)$ problem of the particle interaction (Ref.25).

3.3. Coupling algorithm

The computational domain consists of two parts: Eulerian domain and Lagrangian domain, as is shown in Figure 2. The Eulerian domain is covered only by near-body grids with lifting bodies, thus significantly reducing the computational load. The Lagrangian domain includes not only the lifting bodies but also the shed wake elements.

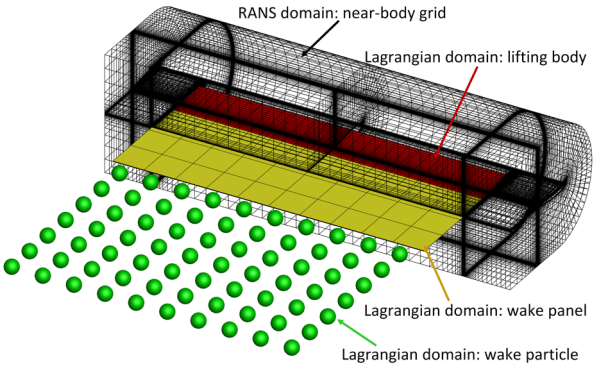

Figure 2: Schematic of the computational domain

The data transition from Eulerian domain to Lagrangian domain follows Kutta-Joukowski theorem. The sectional aerodynamic loads of the lifting bodies are integrated from the RANS surface solution and are transformed into bound vortex strength of lifting line elements by

$$\Gamma = -\frac{1}{2}u_{\text{rel}}cC_l \tag{6}$$

where $C_l = \frac{L}{\frac{1}{2}\rho u_\infty^2 c}$ and $u_{\text{rel}} = u_\infty - u_b + u_i$.

The computation of Γ requires an interactive procedure similar to the loosely coupled algorithm in Ref.26. The circulation is initialized considering a relative velocity of $u_\infty - u_b$. This allows to calculate the induced velocity and hence to update u_{rel}. The difference between the present hybrid method and Ref.26 is that the C_l is here extracted from the Eulerian computation and remains constant during the iterative procedure.

In return, the induced velocity from all the Lagrangian domain (lifting line elements and vortex particles) corrects the interface boundary of the RANS grids, where the characteristic boundary condition using ghost cells are employed to avoid reflection, following the equations below:

$$\begin{cases} \vec{u} = \vec{u}_\infty - \vec{u}_g + \vec{u}_i \\ a^2 = a_\infty^2 + \frac{\gamma-1}{2}(u_\infty^2 - u^2) \\ p = p_\infty \left(\frac{a^2}{a_\infty^2}\right)^{\frac{\gamma}{\gamma-1}} \\ \rho = \rho_\infty \left(\frac{a^2}{a_\infty^2}\right)^{\frac{1}{\gamma-1}} \\ e = \frac{p}{\gamma-1} + \frac{1}{2}\rho u^2 \end{cases} \quad (7)$$

In addition, the hybrid method is parallelized based on a hybrid MPI-OpenMP master-only style to retain the acceleration characters from its parent codes.

The flowchart of the hybrid solver is shown in Figure 3.

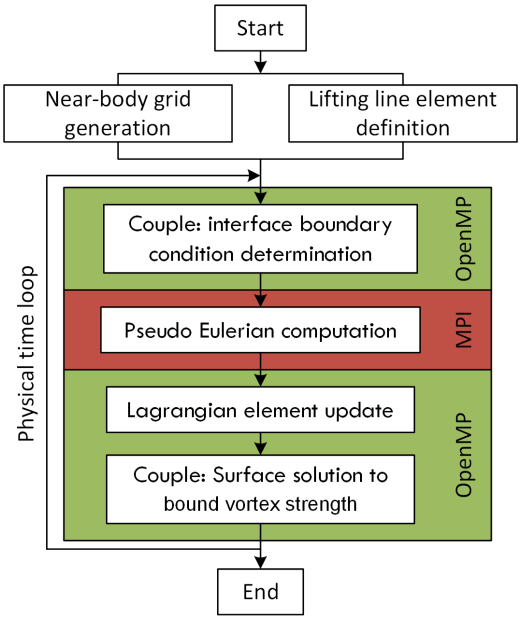

Figure 3: flowchart of the hybrid solver

4. RESULTS AND DISCUSSION

4.1. Wing NACA0015

The static NACA0015 semi-span wing, designed by McAlister and Takahashi (Ref.27), was proved to be a relatively simple and effective case to give insights into the formation and maturation process of trailing vortex from rotor blades. In their experiment, different wing geometries (aspect ratio, chord length, tip type) and different operation conditions (AOA and Re) were combined, and the pressure data on the wing and the velocity across the vortex trailing downstream from the tip were extracted. This particular model has become a widely used benchmark test for novel CFD solvers (Ref.28), with focus on preventing vortex dissipation.

In the current study, the square-tip wing with the aspect ratio of 6.6 and the chord length of 0.52m under an operation condition of AOA = 12° and Re = 1.5 × 10^6 is selected. It is important to note that an additional 0.51° of AOA has been introduced to compensate for the closed-tunnel wall effect.

The pure RANS simulation is firstly carried out using a grid system consisting of a Cartesian FBG, a Cartesian NBG and a C-H body-fitted grid, as is shown in Figure 4. The body-fitted grid extends approximately 1.0c outwards from the wing surface in all directions, and the first layer thickness is set to 1 × 10^{-5}c to ensure y+ < 1. To check the grid independence, three body-fitted grids with different spatial resolution are generated and the medium one with 234×64×64 nodes on the wing surface is found to achieve a satisfactory resolution for sectional pressure distribution and used for hybrid simulation.

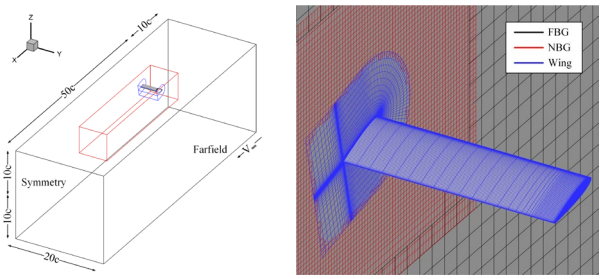

Figure 4: Wing NACA0015: computational domain and overset grids for pure RANS simulation

For the Lagrangian part of hybrid method, the semi-wing is modelled into 33 lifting line elements uniformly. A relatively large time step $\Delta t = 0.75$ with 200 steps and maximum 30 pseudo time steps in each physical time step is chosen in consideration of efficiency. A sensitivity study is performed on the number of rows

of wake panels and the overlapping ratio of particles to ensure the consistency of the intensity of trailing vortex at 1c behind the trailing edge between the Eulerian and Lagrangian parts. Same parameters are also used in DUST computation, and the aerodynamic table in c81 format is prepared with Xfoil (Ref.29).

The spanwise sectional lift and drag coefficients computed by the three solvers are compared with the experimental result in Figure 5. It can be seen that the hybrid solver underestimates the spanwise Cl, which is aligned with the ROSITA solution, and a slight but acceptable difference is found in spanwise Cd. On the other hand, although DUST gives a better spanwise Cl, the outboard Cl becomes less smooth and Cd deviates from the experimental results significantly due to the simplicity of the 2D lifting line theory.

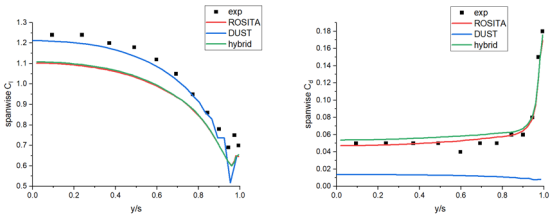

Figure 5: Wing NACA0015: sectional lift and drag coefficients along the wingspan

Figure 6(a) shows the sectional pressure distribution at y/span=0.974 and 0.994. At section y/span=0.974, the hybrid result agrees well with the ROSITA result and the experimental data points, inheriting the errors of the pure RANS computation as well. At section y/span=0.994, a minor gap between the ROSITA and hybrid solver is found from 0.4c backward, which is the result of a slight difference in pressure field at the blade tip, as shown in figure 6(b) where color isolines refer to ROSITA predictions and black isolines refer to hybrid predictions.

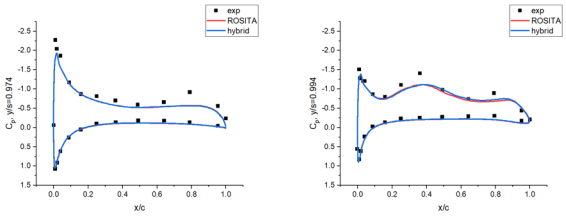

(a) Sectional pressure at y/span=0.974 and 0.994

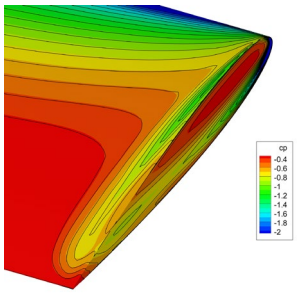

(b) Pressure distribution at blade tip

Figure 6: Wing NACA0015: pressure distribution at tip

The trailing vortex is visualized in Figure 7 truncated by Q-criteria=0.005. It is clear that because of a relatively coarse NBG, the trailing vortex in the RANS calculation dissipates so quickly that the isolated Q surface only extends approximately 2.5c. On the contrary, the hybrid solver preserves the trailing vortex well with the oscillation of the starting vortex.

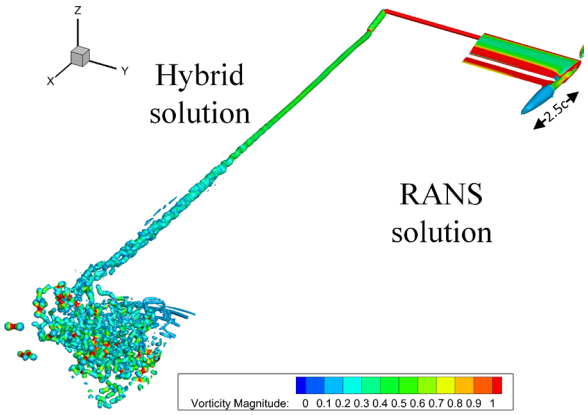

Figure 7: Wing NACA0015: trailing vortex visualization

To quantify the vortex preservation of the hybrid solver, the maximum vertical velocities within the trailing vortex at seven downstream stages are presented in Figure 8.

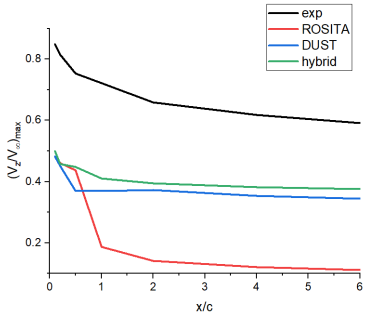

Figure 8: Wing NACA0015: downstream maximum vertical velocity within the trailing vortex

At x/c=0.1 stage, the maximum vertical velocity produced by ROSITA and hybrid solver is only approximately 57% of the experimental value. The velocity in the RANS calculation downpours swiftly by 61.3% at x/c=1.0 because the grid spacing of NBG is set to 0.1c. In contrast, the hybrid solution shows little dissipation, and the maximum vertical velocity only decreases 8.4% from x/c=1.0 to x/c=6.0, which is similar to the DUST solution. Therefore, the hybrid solver demonstrates a good performance on computation accuracy and vorticity preservation for further investigation.

4.2. Caradonna-Tung rotor in hover

The isolated Caradonna-Tung rotor in hover is a well-documented benchmark case (Ref.30). The rotor operates at a tip Mach number of 0.877 and has a collective pitch of 8° and a pre-cone of 0.5°. The body-fitted blade grid has 137×77×37 nodes in each direction totaling 1.01M nodes. The steady ROSITA simulation employs an overset grid system of 5.86M nodes, including a NBG of 2.91M nodes and a FBG of 0.93M nodes. The maximum grid spacing near the rotor rotational plane is 0.1c to resolve the near-field wake. Froude boundary condition (Ref.31) is used to avoid flow recirculation. For unsteady hybrid and DUST computation, each blade is modelled into 20 lifting line elements divided uniformly. The overlapping ratio of particles is 1.2. To achieve a steady condition, both solvers require 10 revolutions with 60 physical steps per revolution, and each physical step includes 30 pseudo time steps in hybrid computation.

Figure 9 demonstrates the coupling effectiveness of the hybrid solver. The wake vortex is consistently convected into and out of the Eulerian grid along with the vortex particles, thanks to the induced velocity applied at the outer boundary of the grids. No wave reflection is observed at the grid boundaries, see Figure 10, indicating the robustness of the characteristic boundary condition.

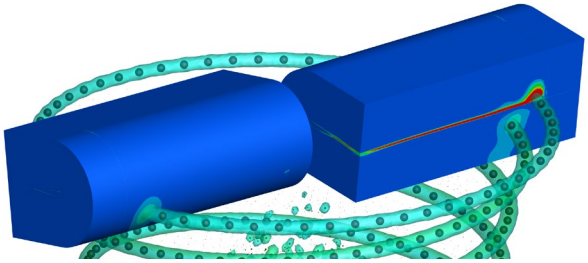

Figure 9: Caradonna-Tung rotor: coupling effectiveness of the Eulerain and Lagrangian domain in respect of wake vortex

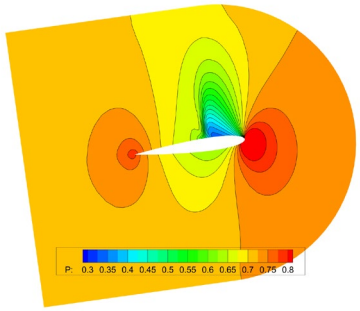

Figure 10: Caradonna-Tung rotor: pressure distribution at section r/R=0.89

In Figure 11, the spanwise lift coefficient computed by the three solvers is compared. The ROSITA solver overestimates the spanwise lift coefficient, while DUST provides a better prediction. The difference between the two parental solvers leads to a mild deviation in the hybrid solution with respect to the RANS solution, which may stem from inaccuracies in the induced velocities at the interface of Eulerian grid. Specifically, the near-field induced velocities are largely composed of those from the lifting line elements, which provide a coarse representation of the blade geometry.

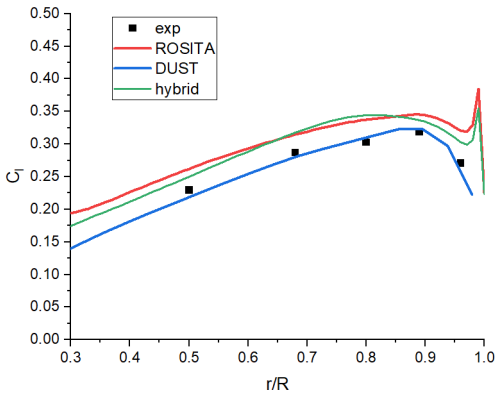

Figure 11: Caradonna-Tung rotor: spanwise sectional lift coefficient

To further investigate this error, Figure 12 shows the sectional pressure distribution at four radial positions produced by ROSITA and hybrid solver. Generally both of them agree well with the experimental results. At tip region, for example, r/R=0.96, the shock location of the hybrid solution is predicted a bit more accurately than RANS one, resulting in a slightly smaller lift coefficient.

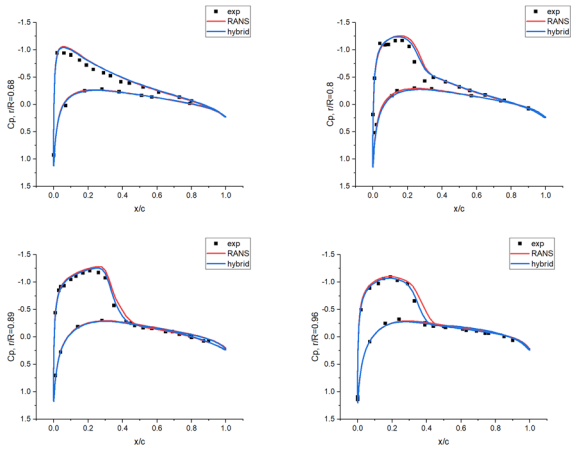

Figure 12: Caradonna-Tung rotor: sectional pressure distribution

The wake of the ROSITA and hybrid solutions is visualized in Fig. 13 (left) using Q-criteria = 0.1. ROSITA captures no more than one revolution of the rotor wake, whereas the hybrid solver fully presents the wake, including the near-field helicoidal structure and the far-field breakdown of the initial starting ring vortex. Figure 13 (right) shows the vorticity contour perpendicular to the blade span across the rotation center. The ROSITA result is supplied by the overset background grid. As the vortices convect downstream, significant numerical diffusion occurs, especially at the interface where grid density changes. Ref.32 indicates that a grid size of 0.005c is essential for improvement, but the computational cost is extremely high. However, the hybrid solver exhibits better performance in tracking the far wake.

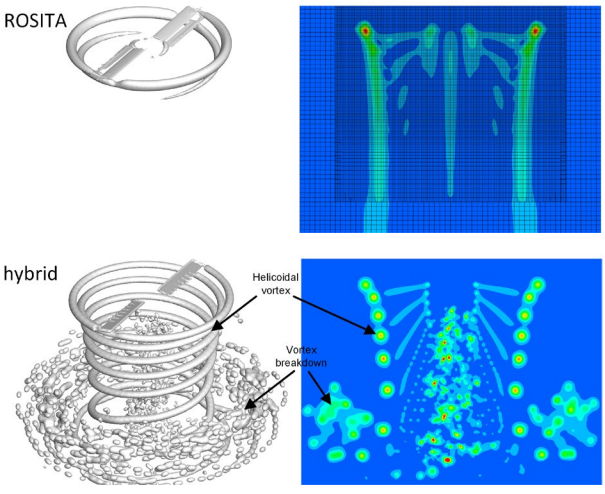

Figure 13: Caradonna-Tung rotor: wake visualization

The computation time for the hybrid solver to rotate 10 revolutions is 60% of the time required for 20k pseudo-time steps of a converged RANS computation, demonstrating the efficiency of the hybrid solver even if the unsteady simulation is carried out for a steady case.

4.3. AH-1G main rotor in low-speed forward fight

The main rotor of AH-1G cobra helicopter in forward fight is reported in TAAT performed in NASA Ames Research Center (Ref.33). The rotor has two untapered rectangular blades with a linear twist of -10°. The radius of the “gloved instrumented blade” is 6.7m and the chord is 0.727m. The blade root is cut at 0.18R. Selected operation condition is test point 2157. The advancing airspeed is 82 knot and the rotor rotation speed is 315.9 rpm, resulting in a tip Mach number of 0.65 and an advance ratio of 0.19. The precone and shaft tilt angles are set to 0°. The blade pitch and flap motion are controlled by the following equations:

$$\begin{cases} \theta(\psi) = 6.0 + 1.2\cos\psi - 5.0\sin\psi \\ \beta(\psi) = 2.13\cos\psi - 0.15\sin\psi \end{cases} \tag{8}$$

The dimension of the body-fitted blade grid is 233×94×53 with 2.33M nodes in total. Cartesian NBG and FBG grids are also generated, and the number of total nodes of the overset grid system is 14.5M for ROSITA computation. The blade is modelled into 40 lifting line elements refined at tip region for hybrid and DUST computation. The particle overlapping ratio is set to 1.3. All the simulations are performed for 5 revolutions and each revolution has 72 physical time steps which is a compromise between the Eulerian and Lagragian methods. In each physical step, there are 50 pseudo steps for ROSITA and hybrid computation.

The prediction of the normal force coefficient at radial sections of r/R = 0.75, 0.86, 0.91, and 0.96 is shown in Figure 14. Both the ROSITA and hybrid solvers produce reliable results compared to experimental data. Discrepancies are primarily observed at azimuth angles around 90° and between 300° and 340°, where the blade strongly interacts with the tip vortex.

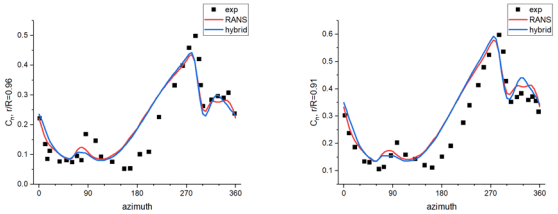

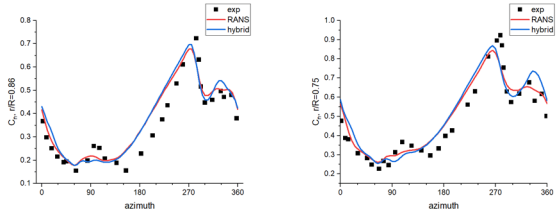

Figure 14: AH-1G main rotor: normal force coefficient

Figure 15 compares the tip vortex trajectories by Q-criteria=0.01 (coloured by vorticity magnitude) of the rotor wake system from ROSITA and hybrid solver. The ROSITA solution only maintains about 2-revolution wake while the hybrid solver preserves the whole of it with little dissipation of the vorticity magnitude thanks to the coupled Lagrangian method.

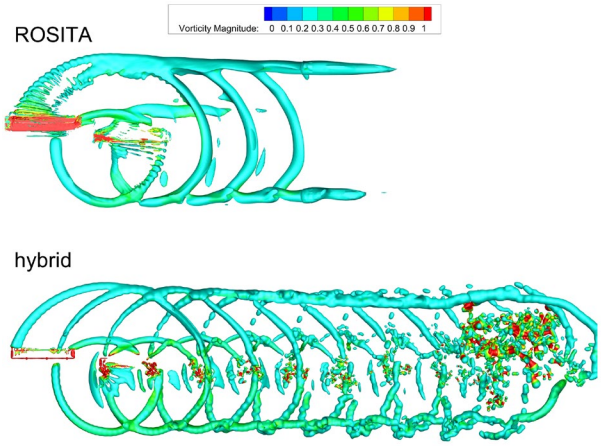

Figure 15: AH-1G main rotor: wake visualization

Furthermore, during the hybrid simulation, 16 out of 64 cores are activated for Lagrangian part and the tagger process of CHIMERA is not necessary, saving 48% of the computational time.

5. CONCLUSIONS

1. Based on the comparative analysis of blade/wing loads with experimental results, it can be concluded that the hybrid solver is capable of simulating complicated blade-vortex interference and has the potential to be applied to more severe cases, including rotor-rotor interactions.
2. The hybrid solver entirely inherits the vortex preservation characteristic of VPM and largely overcomes the numerical diffusion of RANS solver.
3. The hybrid solver also inherits the accuracy of the RANS solver for vortex generation at the blade tip: care is needed to provide sufficient grid resolution to allow for a correct vortex generation.
4. The hybrid solver has advantages of computational efficiency for rotorcraft simulation, even if the original case is steady.

Author contact:

Yi Yuan yi.yuan@polimi.it

Luigi Vigevano luigi.vigevano@polimi.it

6. ACKNOWLEDGMENTS

The authors acknowledge the computation resource of high-performance cluster CFDHub at Politecnico di Milano. The author Yi Yuan would like to thank the China Scholarship Council for financial support under the Grant No. 202006250025.

7. REFERENCES

1. Jespersen, D., Pulliam, T., and Buning, P., “Recent Enhancements to OVERFLOW,” 35th Aerospace Sciences Meeting and Exhibit, Reno, NV, January 1997.
2. Steijl, R., Barakos, G., and Badcock, K., “A Framework for CFD Analysis of Helicopter Rotors in Hover and Forward Flight,” *International Journal for Numerical Methods in Fluids*, Vol. 51, (8), 2006, pp. 819-847. DOI: 10.1002/fld.1086.
3. Biava, M., and Vigevano, L., “Simulation of a Complete Helicopter: A CFD Approach to the Study of Interference Effects,” *Aerospace Science and Technology*, Vol.19, (1), 2012, pp. 37-49. DOI: 10.1016/j.ast.2011.08.006.
4. Srinivasan, G. R., McCroskey, W. J., and Baeder, J. D., “Aerodynamics of Two-dimensional Blade-vortex Interaction,” *AIAA Journal*, Vol. 24, (10), 1986, pp. 1569-1576. DOI: 10.2514/3.9486.
5. Benek, J. A., Buning, P., and Steger, J. L., “A 3-D Chimera Grid Embedding Technique,” 7th Computational Physics Conference, Cincinnati, OH, July 1985. DOI: 10.2514/6.1985-1523.
6. Dehaeze, F., and Barakos, G. N., “Mesh Deformation Method for Rotor Flows,” *Journal of Aircraft*, Vol. 49, (1), 2012, pp.82-92. DOI: 10.2514/1.C031251.
7. Dindar, M., Lemnios, A., Shephard, M., Flaherty, J., and Jansen, K., “An Adaptive Solution Procedure for Rotorcraft Aerodynamics,” 16th AIAA

Applied Aerodynamics Conference, Albuquerque, NM, June 1998. DOI: 10.2514/6.1998-2417.

8. Yeshala, N., Egolf, A., Vasilescu, R., and Sankar, L., “Application of Higher Order Spatially Accurate Schemes to Rotors in Hover,” 24th AIAA Applied Aerodynamics Conference, San Francisco, CA, June 2006.

9. Steinhoff, J., Wenren, Y., and Caradonna, F. X., “Application of Vorticity Confinement to Rotorcraft Flows,” 31st European Rotorcraft Forum, Florence, September 2005.

10. Landgrebe, A. J., Moffitt, R. C., and Clark, D. R., “Aerodynamic Technology for Advanced Rotorcraft - Part I,” *Journal of the American Helicopter Society*, Vol. 22, (2), 1977, pp.21-27. DOI: 10.4050/JAHS.22.21.

11. Colmenares, J. D., López, O. D., and Preidikman, S., “Computational Study of A Transverse Rotor Aircraft in Hover Using the Unsteady Vortex Lattice Method,” *Mathematical Problems in Engineering*, Vol. 2015, (1), 2005, pp.478457. DOI: 10.1155/2015/478457.

12. Wachspress, D. A., Quackenbush, T. R., and Boschitsch, A. H., “Rotorcraft Interactional Aerodynamics with Fast Vortex/fast Panel Methods,” *Journal of the American Helicopter Society*, Vol. 48, (4), 2003, pp.223-235. DOI: 10.4050/JAHS.48.223.

13. Leishman, J. G., Bhagwat, M. J., and Bagai, A., “Free-vortex Filament Methods for the Analysis of Helicopter Rotor Wakes,” *Journal of Aircraft*, Vol. 39, (5), 2002, pp.759-775. DOI: 10.2514/2.3022.

14. Zhao, J., and He, C., “A Viscous Vortex Particle Model for Rotor Wake and Interference Analysis," *Journal of the American Helicopter Society*, Vol. 55, (1), 2010, pp.12007. DOI: 10.4050/JAHS.55.012007.

15. Zanotti, A., Savino, A., Palazzi, M., Tugnoli, M., and Muscarello, V., “Assessment of A Mid-fidelity Numerical Approach for the Investigation of Tiltrotor Aerodynamics,” *Applied Sciences*, Vol. 11, (8), 2021, pp.3385. DOI: 10.3390/app11083385.

16. Wang, L., Xu, G., and Shi, Y., “Development and Validation of a Hybrid Method for Predicting Helicopter Rotor Impulsive Noise,” *Proceedings of the Institution of Mechanical Engineers, Part G: Journal of Aerospace Engineering*, Vol. 233, (4), 2018, pp.1323-1339. DOI: 10.1177/0954410018756476.

17. He, C., and Rajmohan, N., “Modeling the Aerodynamic Interaction of Multiple Rotor Vehicles and Compound Rotorcraft with Viscous Vortex Particle Method,” American Helicopter Society 27th Annual Forum Proceedings, West Palm Beach, FL, May 2016.

18. Moushegian, A. M., and Smith, M. J., “Dual-Solver Hybrid Computational Approach to Integrated Propulsion Aerodynamics,” *Journal of Aircraft*, Vol. 60, (2), 2023, pp.521-532. DOI: 10.2514/1.C036808.

19. Spalart, P., and Allmaras, S., “A One-equation turbulence Model for Aerodynamic Flows,” 30th Aerospace Sciences Meeting and Exhibit, Reno, NV, January 1992. DOI: 10.2514/6.1992-439.

20. Roe, P. L., “Approximate Riemann Solvers, Parameter Vectors, and Difference schemes,” *Journal of Computational Physics*, Vol. 43, (2), 1981, pp.357-372. DOI: 10.1016/0021-9991(81)90128-5.

21. Venkatakrishnan, V., “On the Accuracy of Limiters and Convergence to Steady State Solutions,” 31st Aerospace Sciences Meeting, Reno, NV, January 1993. DOI: 10.2514/6.1993-880.

22. Jameson, A., “Time Dependent Calculations Using Multigrid, with Applications to Unsteady Flows Past Airfoils and Wings,” 10th Computational fluid dynamics conference, Honolulu, HI, June 1991. DOI: 10.2514/6.1991-1596.

23. Chesshire, G., and Henshaw, W. D., “Composite Overlapping Meshes for the Solution of Partial Differential Equations,” *Journal of Computational Physics*, Vol. 90, (1), 1990, pp.1-64. DOI: 10.1016/0021-9991(90)90196-8.

24. Tugnoli, M., Montagnani, D., Syal, M., Droandi, G., and Zanotti, A., “Mid-fidelity Approach to Aerodynamic Simulations of Unconventional VTOL Aircraft Configurations,” *Aerospace Science and Technology*, Vol. 115, 2021, pp.106804. DOI: 10.1016/j.ast.2021.10.6804.

25. Lindsay, K., and Krasny, R., “A particle method and adaptive treecode for vortex sheet motion in three-dimensional flow,” *Journal of*

Computational Physics, Vol.172, (2), 2001, pp.879-907. DOI: 10.1006/jcph.2001.6862

26. Gallay, S., and Laurendeau, E., "Nonlinear Generalized Lifting-line Coupling Algorithms for Pre/poststall Flows," *AIAA Journal*, Vol. 53, (7), 2015, pp.1784-1792. DOI: 10.2514/1.J053530.

27. McAlister, K. W., Takahashi, R. K., "NACA 0015 Wing Pressure and Trailing Vortex Measurements," NASA TP 3151, 1991.

28. Fu, J., Yuan, Y., and Vigevano, L., "Numerical Investigations of the Vortex Feature-based Vorticity Confinement Models for the Assessment in Three-dimensional Vortex-dominated Flows," Meccanica, Vol. 57, (7), 2022, pp.1657-1676. DOI: 10.1007/s11012-022-01525-5.

29. Drela, M., "XFOIL: An Analysis and Design System for Low Reynolds Number Airfoils," Low Reynolds Number Aerodynamics, Notre Dame, IN, June 1989.

30. Caradonna, F. X., and Tung, C., "Experimental and Analytical Studies of a Model Helicopter Rotor in Hover," NASA TM 81232, 1981.

31. Biava, M., and Vigevano, L., "The Effect of Far-field Boundary Conditions on Tip Vortex Path Predictions in Hovering," CEAS Aerospace Aerodynamics Research Conference, Cambridge, June 2002.

32. Han, S., Song, W., Han Z., "A Novel High-order Scheme for Numerical Simulation of Wake Flow over Helicopter Rotors in Hover," *Chinese Journal of Aeronautics*, Vol. 35, (5), 2022, pp.260-274. DOI: 10.1016/j.cja.2021.07.032.

33. Cross, J. L., and Watts, M. E., "Tip Aerodynamics and Acoustics Test: A Report and Data Survey," NASA RP 1179, 1988.

8. CLASSIFICATION & COPYRIGHT

The paper must be unclassified for release to the public and cleared by the appropriate company and/or government agency if necessary. CEAS and its national member societies shall be allowed to publish the paper. The copyright information is stated on the Forum website https://www.rotorcraft-forum.eu/ and on the front page of this template. All papers presented at the ERF will be published as ERF proceedings. In addition they will be available in a freely accessible web-based repository 2 years after the respective conference.